RSC Advances

PAPER

View Article Online
View Journal | View Issue

Cite this: *RSC Adv.*, 2026, **16**, 9264

Synthesis and microstructural properties of Pt-decorated α-Fe_2O_3 nanotubes for hydrogen gas sensing applications

Monika Šoltić,[a] Maria Gracheva,[bc] Nikola Baran,[a] Goran Dražić,[d] Robert Peter,[e] Károly Lázár,[b] Goran Štefanić,[a] Marijan Marciuš,[f] Nikolina Novosel,[g] László Ferenc Kiss,[h] Matthijs A. van Spronsen,[i] Mile Ivanda,[a] Zoltán Klencsár*[b] and Marijan Gotić*[a]

Pt-free and Pt-decorated α-Fe_2O_3 nanotubes containing 1 and 5 mol% Pt were hydrothermally synthesized to investigate how Pt decoration influences low-temperature hydrogen sensing beyond simple catalytic enhancement. Unlike many previous studies that focus primarily on sensing performance, this work correlates Pt-induced microstructural and magnetic ordering with sensor behavior. Structural characterization confirmed retention of the hematite phase after Pt modification, while XPS revealed both metallic and oxidized Pt species, along with an increased concentration of surface oxygen species. Mössbauer spectroscopy, EPR, and magnetic measurements showed that Pt decoration, assisted by heat treatment, partially restores the Morin transition and improves magnetic ordering, which directly correlates with the observed enhancement in sensing performance. Compared to Pt-free hematite, Pt-decorated nanotubes exhibited significantly improved hydrogen detection, achieving a detection limit of 1.0 ppm at 463 K with a fast response of 3.6 s. Notably, efficient sensing was achieved at lower operating temperatures (down to 363 K), with only 1 mol% Pt required to obtain high sensitivity and rapid response. Measurements performed in nitrogen further revealed enhanced responses due to reduced oxygen competition and promoted hydrogen spillover on Pt sites. These results demonstrate that Pt decoration of reducible α-Fe_2O_3 nanotubes links structural and magnetic ordering with hydrogen sensing performance, providing guidance for the rational design of advanced hydrogen sensors.

Received 17th November 2025
Accepted 10th February 2026

DOI: 10.1039/d5ra08865h

rsc.li/rsc-advances

1. Introduction

Platinum (Pt) on reducible metal oxide supports represents an important class of materials with diverse applications, particularly in catalysis and energy conversion.[1,2] The synergistic interaction between platinum and the metal oxide support has been extensively studied to improve catalytic and sensing performance, stability and selectivity. Decorating metal oxide surfaces with platinum nanoparticles enables the development of materials with customized properties for applications such as fuel cells,[3] sensors[4] and environmental remediation.[5] Metal oxides also act as robust supports that improve Pt dispersion and stability. Radin *et al.* showed that Pt forms highly visible nanoparticles on the hematite surface, while in SnO_2, Pt tends to form intermetallic Pt_xSn_y compounds at relatively low annealing temperatures, highlighting how the chemical properties of the metal oxide support affect Pt dispersion, which is crucial for optimizing catalytic and sensing applications.[6] Among various platinum metal oxide systems, Pt/α-Fe_2O_3 has attracted particular interest. α-Fe_2O_3 (hematite) is a stable, abundant and environmentally friendly semiconductor with notable photochemical activity and adsorption capability.[7,8] When decorated with Pt, its catalytic[1,9] and photocatalytic performance[10] are significantly enhanced, making it useful for water splitting, pollutant degradation and oxidation reactions.[10]

Hematite can be synthesized in various morphologies, including nanotubes,[11] hollow spheres,[12] nanorings[13] and

[a]*Laboratory for Molecular Physics and Synthesis of New Materials, Division of Materials Physics, Ruđer Bošković Institute, Bijenička cesta 54, 10 000 Zagreb, Croatia. E-mail: gotic@irb.hr*

[b]*Budapest Neutron Centre, Institute for Energy Security and Environmental Safety, HUN-REN Centre for Energy Research, Konkoly-Thege Miklós út 29-33, 1121 Budapest, Hungary. E-mail: klencsar.zoltan@ek.hun-ren.hu*

[c]*Institute of Chemistry, ELTE Eötvös Loránd University, Pázmány Péter s. 1/A, 1117 Budapest, Hungary*

[d]*National Institute of Chemistry, Hajdrihova, 19, SI-1001, Ljubljana, Slovenia*

[e]*University of Rijeka, Faculty of Physics and Centre for Micro- and Nanosciences and Technologies, Radmile Matejčić 2, Rijeka, Croatia*

[f]*Laboratory for the synthesis of new materials, Division of Materials Chemistry, Ruđer Bošković Institute, 10000 Zagreb, Croatia*

[g]*Institute of Physics, Bijenička cesta 46, 10000 Zagreb, Croatia*

[h]*Institute for Solid State Physics and Optics, HUN-REN Wigner Research Centre for Physics, Konkoly-Thege Miklós út 29-33, 1121 Budapest, Hungary*

[i]*Diamond Light Source Ltd, Oxfordshire, UK*

urchin-like[14] nanostructures. Among these, nanotubes are particularly promising due to their quasi-one-dimensional morphology and remarkable chemical and magnetic properties, which make them excellent supports for Pt nanoparticles. Jia *et al.*[11] developed a one-step hydrothermal synthesis method to produce highly crystalline and uniform hematite nanotubes through a phosphate ion-assisted dissolution mechanism, allowing precise control of morphology. Hu *et al.*[13] and Dražić *et al.*[15] have also shown that introducing phosphate ions during synthesis plays a crucial role in controlling the nucleation and growth of hematite crystals and facilitates the formation of advanced morphologies such as nanorings. These morphologies are particularly attractive for gas sensing applications because they provide efficient charge transport pathways, enhanced gas diffusion, and a high density of accessible surface sites for surface reactions.

The magnetic properties of hematite depend strongly on its morphology and particle size, which affect magnetic anisotropy and coercivity. Changes in magnetic ordering in hematite are often associated with modifications in electronic structure and defect chemistry, which can directly influence charge transport and gas sensing behavior.[16–22] In addition to its magnetic properties, hematite's semiconducting nature makes it an excellent candidate for gas sensing applications. Nanostructures with well-defined geometries, such as nanotubes and nanorings, exhibit enhanced surface reactivity and gas diffusion.[11,13] Hydrogen and other reducing gases (CO, NH_3) are of particular concern due to their toxicity and flammability, highlighting the need for reliable detection technologies.[23] Metal oxide semiconductors (MOS) are widely used for hydrogen detection due to their high sensitivity, long-term stability and cost-effectiveness.[24] Recent research has also focused on various MOS for hydrogen sensing applications, including SnO_2,[25,26] WO_3,[27,28] TiO_2 (ref. 29) and ZnO.[30]

Hematite nanostructures have attracted increasing attention for gas sensing due to their n-type conductivity, stability, tunable morphology, low cost, low power consumption and ease of integration into practical devices.[31,32] Zhang *et al.* demonstrated that hollow sea urchin-like α-Fe_2O_3 nanostructures exhibit higher sensitivity to reducing gases than nanocubes or irregular nanoparticle aggregates, attributed to enhanced surface area and gas diffusion.[14] In addition, Fe_2O_3-based heterostructures with controlled nanocrystal morphology have been shown to exhibit enhanced hydrogen sensing performance due to synergistic interfacial effects and increased specific surface area, as seen in γ-Fe_2O_3/α-Fe_2O_3 and Fe_2O_3/In_2O_3 systems.[33,34] Moreover, Mirzaei *et al.* reviewed α-Fe_2O_3 gas sensors and identified morphology as a key factor influencing sensitivity and selectivity, although high operating temperatures (>473 K) and long recovery times remain challenges.[23] Similarly, Nakatani and Matsuoka showed that hematite has low sensitivity to reducing gases due to the absence of reversible oxidation–reduction reactions.[35] To address these limitations, noble metal decoration (Pt, Pd) has been widely used to improve sensor performance through mechanisms such as the spillover effect and electronic sensitization, whereby noble metal nanoparticles provide additional active sites for gas adsorption and accelerate the interaction of H_2 with adsorbed oxygen species.[23,36,37]

Surface modification strategies can significantly enhance gas adsorption and charge transfer.[38] For example, Zhang *et al.* showed that Pt-decorated Fe_2O_3 nanosheets exhibit much higher hydrogen sensitivity, faster response, and superior stability compared with Pt-free Fe_2O_3.[39] Similar enhancements from noble metal decoration have also been reported for other metal oxide semiconductors, including ZnO systems decorated with Ir, Ru, and Ir–Ru alloys,[40] SnO/SnO_2 nanosheets modified with Pd/Ag alloy nanoparticles,[41] and Pd-coated TiO_2 nanotubes.[42] This is consistent with our previous work, in which Pt-decorated hematite nanoparticles with irregular morphology showed improved hydrogen sensing.[4]

Despite extensive studies on Pt-decorated metal oxides and hematite-based sensors, a systematic correlation between morphology-controlled microstructure, magnetic ordering and hydrogen sensing behavior remains scarce. In this work, Pt-decorated α-Fe_2O_3 nanotubes are investigated as model sensing materials due to their chemical stability, reducible nature, and well-defined nanotubular morphology, which enables reproducible synthesis and a systematic investigation of how structural features influence material behavior. Unlike our previous study,[4] in which Pt was mechanochemically dispersed on α-Fe_2O_3 with limited morphological control, hydrothermally synthesized nanotubes are used here as structured supports and decorated with Pt nanoparticles *via* wet impregnation. The selected Pt loadings (1 and 5 mol%) allow controlled evaluation of the influence of Pt dispersion on hydrogen sensing performance while maintaining reproducibility and minimizing noble metal content. This approach enables systematic insight into correlations between microstructural features, magnetic ordering, and hydrogen sensing behavior. Furthermore, sensing measurements are conducted in both air and nitrogen atmospheres to clarify the influence of ambient oxygen on sensor response and to gain deeper insight into the sensing mechanism.

2. Experimental

2.1. Chemicals

Iron (III) chloride hexahydrate ($FeCl_3 \cdot 6H_2O$, ≥99% pro-analysis grade (p.a.), Cat. no. 31232-250 G) produced by *Honeywell Fluka*, ammonium dihydrogen phosphate ($NH_4H_2PO_4$, pro-analysis grade (p.a.)) and toluene ($C_6H_5CH_3$, pro-analysis grade (p.a.) Cat. No. 1914401) produced by *Kemika*, platinum (II) acetylacetonate (Pt $(C_5H_7O_2)_2$, 97%, Cat. No. 282782-5G) produced by Sigma-Aldrich, and ethanol absolute (C_2H_6O, ≥99.98%, pro-analysis grade (p.a.)) produced by *GramMol* were used.

2.2. Synthesis procedure

The α- Fe_2O_3 support and the platinum-loaded Fe_2O_3 samples (Pt/α-Fe_2O_3) were synthesized using a hydrothermal method (Jia

et al. 2005). To prepare α-Fe_2O_3, 3.2 mL of aqueous iron (III) chloride solution ($FeCl_3$, 0.5 M) and 2.9 mL of aqueous ammonium dihydrogen phosphate solution ($NH_4H_2PO_4$, 0.02 M) were mixed in a glass flask with a magnetic stirrer. Milli-Q water (MQ-H_2O) was added to adjust the final volume to 80 mL. The mixture was stirred for 15 minutes, then transferred to two 50 mL PTFE-lined stainless-steel autoclaves for hydrothermal treatment at 231 °C for 48 hours. After the procedure, the sample was cooled to room temperature and collected in several cycles by centrifugation and washing with deionized water and ethanol. The sample was dried overnight in a vacuum dryer to obtain powdered hematite (α-Fe_2O_3) with a nanotube morphology, referred to as T-FP0.

The T-FP0 sample was annealed in a tube furnace under a controlled atmosphere. The sample was heated at 200 °C under nitrogen (N_2) gas flow for 1 hour, then heated in air at 380 °C for 2 hours to obtain the annealed hematite sample, referred to as T-$FP0_{ann}$.

To prepare the platinum-loaded samples, 0.1 g of powdered T-FP0 was suspended in 15 mL of ethanol (EtOH) and platinum (II) acetylacetonate ($Pt(acac)_2$) was used as the precursor. For a platinum loading of 1 mol%, 0.0025 g of $Pt(acac)_2$ was dissolved in 5 mL of toluene, for a loading of 5 mol%, 0.0123 g of $Pt(acac)_2$ was dissolved in 5 mL of toluene. The mol% refers to the molar ratio of Pt to Fe_2O_3.The precursor solution was added to the T-FP0 suspension and mixed until the ethanol was completely evaporated. The resulting powder was dried and annealed in a tube furnace at 200 °C under N_2 gas flow for 1 hour, then at 380 °C in air for 2 hours to obtain platinum-dispersed samples. These are referred to as T-FP1 (1 mol% Pt relative to Fe_2O_3) and T-FP5 (5 mol% Pt relative to Fe_2O_3). Details of the sample labeling, including platinum content, amount of added Pt $(acac)_2$ and annealing conditions, are summarized in Table 1.

2.3. Characterization techniques

The structural, compositional, and electronic properties of the synthesized samples were characterized using a combination of complementary techniques. The thermal field emission scanning electron microscope (FE-SEM), atomic resolution scanning transmission electron microscope (AR STEM) and energy dispersive X-ray spectrometry (EDS) were used to analyze the morphology and elemental composition of the samples. The crystal structure was confirmed by X-ray diffraction (XRD), while the surface composition and oxidation states of Fe, Pt, and O were examined by X-ray photoelectron spectroscopy (XPS) and near-edge X-ray absorption fine structure (NEXAFS). Thermal stability was assessed by thermogravimetric and differential scanning calorimetry (TGA/DSC). Magnetic and electronic structures were further investigated by ^{57}Fe Mössbauer spectroscopy, electron paramagnetic resonance (EPR), and SQUID magnetometry. Detailed measurement conditions and data acquisition parameters for all techniques are provided in Sec. S1.1. of the SI.

2.4. Drop casting

To measure the electrical response of the prepared samples, we used interdigitated platinum electrodes (IDE) from Micrux Technologies (model ED-IDE2-Pt, 10/5 μm electrode/gap). Samples were suspended in ethanol (0.01 g in 40 μL) and drop-cast onto the IDE substrates, with 5 μL of the suspension applied to each IDE. To ensure uniformity, we used a custom-built precision drop-casting system, consisting of a heated IDE holder with adjustable axes, a motorized pipette, and a magnifier with adjustable zoom and illumination. The IDE was heated to 328 K and the suspension was sonicated for 2–3 minutes before pipetting from a fixed height of 5 mm. To avoid uneven deposition, the suspension was held in the pipette for no more than 5 seconds. The challenges and limitations of the drop casting method, as well as the optimization procedures are discussed in detail in Šoltić *et al.*[4]

2.5. Gas sensing measurements

The response of the samples to hydrogen gas was measured using a custom-built chamber, based on our previous design, with a heated sample stage.[43] A schematic illustration of the chamber is provided in the SI (Fig. S1). The chamber isolates the sample from the external atmosphere, vibrations, and electromagnetic interference, and was sealed during the measurements. This controlled configuration was intentionally used to minimize external variables and isolate the intrinsic sensing response of the material, enabling reliable investigation of the sensing mechanism. The sample stage includes a heater, thermistor, and gold-plated probes, with the temperature controlled to ±1 K *via* a PC-connected electronic circuit board.

The platinum-plated probes were connected to a Keithley Sourcemeter 2450, which was programmed to deliver a constant current while measuring resistance. After placing the IDE substrate on the heated stage, the chamber was sealed, and the sample was stabilized for ~5 minutes before resistance measurements began. Hydrogen gas (H_2 5.0, 99.999% purity,

Table 1 Labeling of samples, including platinum content, amount of added $Pt(acac)_2$ and annealing conditions

Sample	Platinum content (mol%)	Pt $(acac)_2$ added (*g*)/0.1 g T-FP0	Annealing conditions
T-FP0	0	—	None
T-$FP0_{ann}$	0	—	200 °C (N_2, 1 h) → 380 °C (air, 2 h)
T-FP1	1	0.0025	200 °C (N_2, 1 h) → 380 °C (air, 2 h)
T-FP5	5	0.0123	200 °C (N_2, 1 h) → 380 °C (air, 2 h)

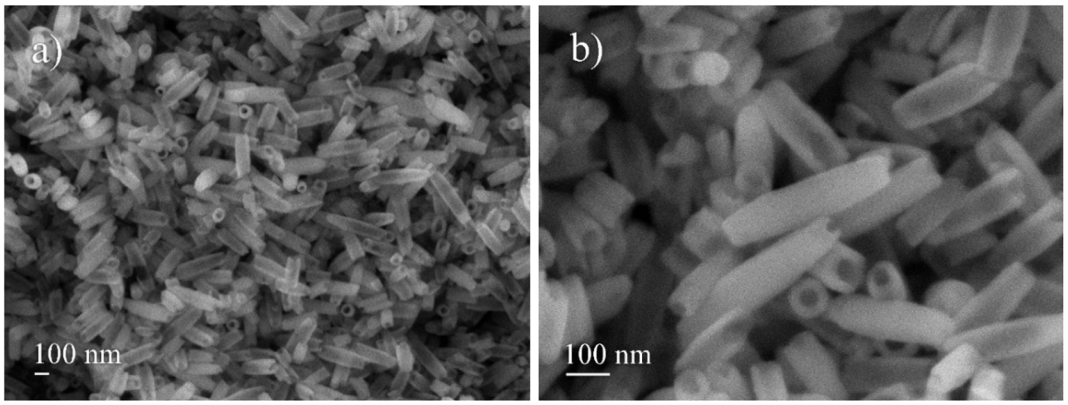

Fig. 1 Scanning electron micrographs of T-FP0 sample taken with secondary electron imaging at an accelerating voltage of 10 kV and magnifications of (a) 330 00× and (b) 1 000 00×.

Messer, Croatia) was used as the target analyte. Specific amounts of H_2 gas were injected into the chamber using a calibrated gas syringe (Hamilton, USA). H_2 was added until saturation became apparent (411 ppm), after which the chamber was ventilated and the procedure repeated. Measurements performed in air were conducted at a relative humidity ranging from approximately 20% to 40%. Nitrogen measurements were carried out under similar conditions, with the relative humidity maintained at around 15%.

The sensor response was calculated as the relative change in electrical resistance, defined as $\Delta R/R_0 = (R - R_0)/R_0$, where R_0 is the initial baseline resistance at a given temperature (before H_2 exposure) and R is the resistance after exposure. The response curves were obtained by plotting $\Delta R/R_0$ as a function of H_2 concentration the corresponding uncertainty was calculated by propagating the standard deviations of R and R_0 using the standard error propagation formula with covariance. This provides a realistic estimate of the total uncertainty in the

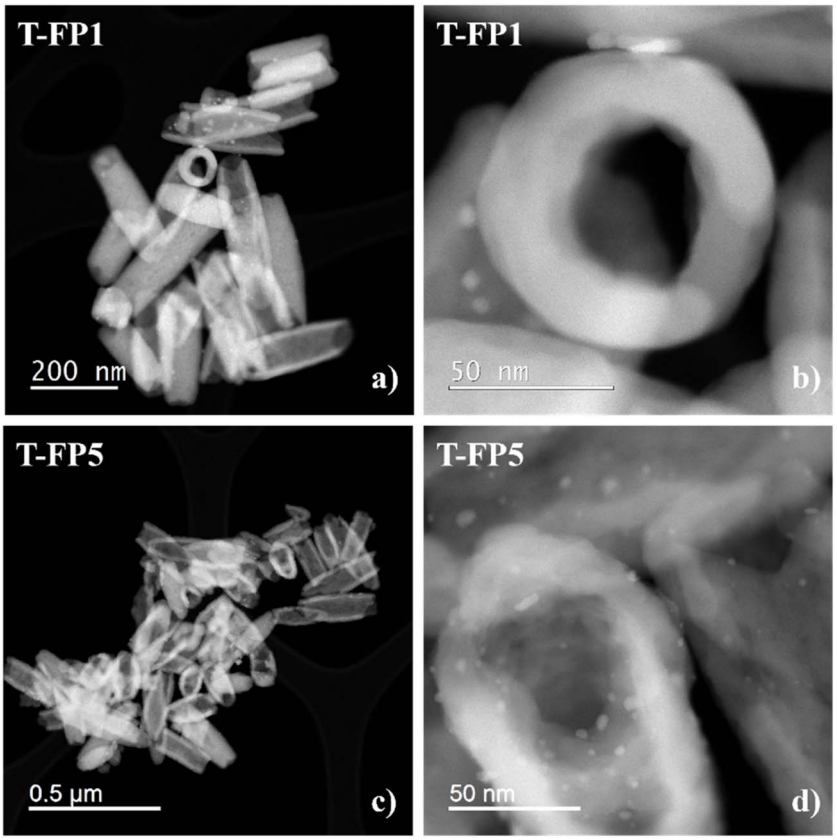

Fig. 2 Dark-field scanning transmission electron micrographs of samples (a and b) T-FP1 and (c and d) T-FP5.

calculated response. Although some measurements had a high standard deviation due to signal noise, the relative error in the calculated response remained within acceptable limits. This approach provides a more accurate estimate of the uncertainty in the response, as it reflects the functional dependence on both variables rather than treating them independently.

The limit of detection (LOD) was defined as the hydrogen concentration corresponding to a signal-to-noise ratio of 3 ($S/N = 3$), estimated by linear interpolation between the nearest data points around the 3σ threshold.

3. Results and discussion

3.1. Structural and elemental results

Fig. 1 shows the morphology of the synthesized T-FP0 sample using scanning electron micrographs (SEM). The images display a well-defined nanotube morphology formed in high yield. The average length of the nanotubes was approximately 249 ± 66 nm, and the average width was about 91 ± 11 nm, with the corresponding statistical size distributions provided in the SI (Fig. S2). Almost all particles appear to be hollow nanotubes, as indicated by their open ends and visible internal cavities.

Fig. 2 shows dark-field scanning transmission electron micrographs of samples (a and b) T-FP1 and (c and d) T-FP5. The resulting STEM-DF images display small bright spots corresponding to platinum (Pt) nanoparticles, confirming the successful decoration of Pt nanoparticles on the surfaces of the α-Fe_2O_3 nanotubes. The size distribution of Pt nanoparticles for the T-FP5 sample, fitted with normal and log–normal functions, is shown in Fig. S3 of the SI. The results indicate that the average Pt nanoparticle size is approximately 2.5 ± 1.2 nm (normal distribution). This analysis was not performed for T-FP1 due to the small number of visible Pt nanoparticles.

Fig. 3 shows a high-resolution scanning transmission electron microscopy (STEM) image (a) of the T-FP5 sample and the corresponding energy-dispersive X-ray spectroscopy (EDXS) elemental mapping. The element maps show the distribution of iron ((Fe K-edge), (b), oxygen (O K-edge (c)) and platinum (Pt L-edge (d)), indicating a uniform dispersion of Fe and O within the nanotubular morphology, with Pt nanoparticles located on the surface. The samples were further analyzed by FESEM/EDS, and their elemental composition (wt% and at%) is provided in Table S1 of the SI.

3.2. XRD results

X-ray diffraction (XRD) confirmed the formation of pure α-Fe_2O_3 in all samples, with no secondary phases detected, indicating that the hydrothermal synthesis and Pt decoration did not alter

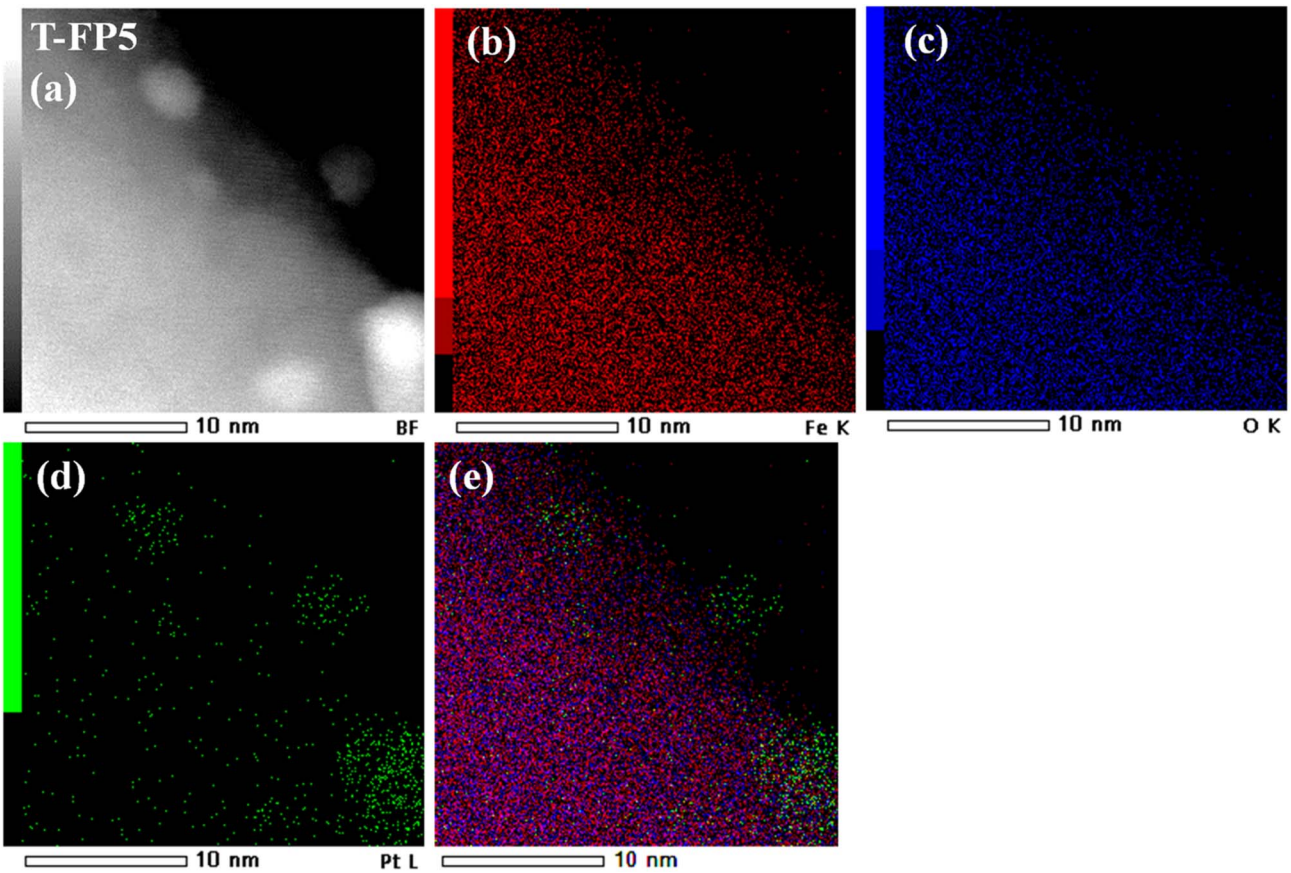

Fig. 3 STEM image of sample T-FP5 (a) and the corresponding EDXS elemental mapping images of the Fe K-peak (b), O K-peak (c), Pt L-peak (d) and the overlay of the Pt L, Fe K and O K (e).

the hematite structure (Fig. S4 and S5, SI). The absence of Pt diffraction lines suggests that the PtNPs are very small and uniformly dispersed on the hematite surface without aggregation. The narrow diffraction peaks further confirm the excellent crystallinity of the samples (Fig. S4 and S5, SI). Rietveld refinement results show that Pt decoration has no significant effect on the hematite lattice parameters, confirming that Pt does not incorporate into the α-Fe_2O_3 crystal lattice but remains on the surface (Table S2, SI). Detailed refinement parameters, diffraction patterns, and quantitative analysis are provided in Sec. S2.2. of the SI.

3.3. XPS results

X-ray photoelectron spectroscopy (XPS) was used to analyze the chemical composition and oxidation states of the elements in samples with 1 mol% (T-FP1) and 5 mol% (T-FP5) Pt loading. The elemental composition of the samples is shown in the wide-scan XPS spectra in Fig. S6 of the SI, where the presence of carbon in the XPS elemental analysis is also discussed in detail. Table 2 shows an increase in Pt content from 0.5% in T-FP1 to 2% in T-FP5.

High-resolution Pt 4f XPS spectra (Fig. 4) of samples T-FP1 and T-FP5 reveal three platinum oxidation states (Pt^0, Pt^{2+} and Pt^{4+}), indicating that Pt exists in both metallic and oxidized forms on the α-Fe_2O_3 surface. The average oxidation states of platinum in the samples are summarized in Table S3 of the SI. The relative distribution of these species is similar in both samples, referring to their proportion rather than the absolute Pt content. The coexistence of multiple oxidation states can be attributed to surface and interfacial effects: metallic Pt^0 forms during thermal decomposition of the Pt precursor, while Pt^{2+} and Pt^{4+} result from surface oxidation and the formation of Pt–O–Fe interfacial bonds. The core of the Pt nanoparticles remains metallic, while the surface is partially oxidized. The Fe^{3+} oxidation state of the hematite support remains unchanged, indicating that charge transfer is confined to the Pt–Fe_2O_3 interface. Detailed peak fitting parameters, binding energies and quantitative analysis are provided in Sec. S.2.3.1. of the SI.

X-ray photoelectron spectroscopy confirmed that iron in all samples is present exclusively as Fe^{3+} in octahedral coordination, characteristic of α-Fe_2O_3, with Fe $2p_{3/2}$ and Fe $2p_{1/2}$ peaks at ~711 eV and ~724 eV, and corresponding satellite features at ~719 eV and ~733 eV (Fig. S7, SI).[39,44–46] Slight deviations from typical hematite spectra may indicate surface hydroxylation.[44] No Fe^{2+} or Fe^0 species were detected, indicating that the oxidation state of iron remains Fe^{3+} after Pt decoration and annealing. The absence of binding-energy shifts in Pt-decorated samples suggests negligible charge transfer between Pt and Fe_2O_3.

The NEXAFS spectra of the Fe-$L_{2,3}$ edges (Fig. S8, SI) further support these results. All spectra are very similar and match the spectrum for α-Fe_2O_3, confirming that neither Pt loading nor annealing alters the Fe oxidation state.[47]

Fig. 5 shows the O 1s XPS spectra of all synthesized samples, while the quantitative distribution of oxygen species is summarized in Fig. S9 of the SI. All spectra confirm the preservation of the hematite structure, with oxygen components consistent with those reported for α-Fe_2O_3-based nanostructures.[39,48,49] The main peak at ~530 eV (blue) corresponds to lattice oxygen (O–Fe), while the component at ~531 eV (grey) is attributed to chemisorbed oxygen species and Pt–O–Fe interfacial bonds. This contribution is most pronounced in T-FP1, while its slightly lower intensity in T-FP5 suggests partial saturation of available Pt–O–Fe interfacial sites at higher Pt loading. A more detailed analysis of the O 1s spectra is provided in Sec. 2.3.3. of the SI. The XPS results show that Pt decoration modifies the hematite surface by stabilizing chemisorbed oxygen and hydroxyl species and promoting Pt–O–Fe bond

Table 2 Elemental composition of samples T-FP1 and T-FP5, determined by XPS analysis, showing atomic percentages of Fe, O, Pt, C, and P

	Fe (%)	O (%)	Pt (%)	C (%)	P (%)
T-FP1	17	66	0.5	15	1.5
T-FP5	20	58	2.0	19	1.0

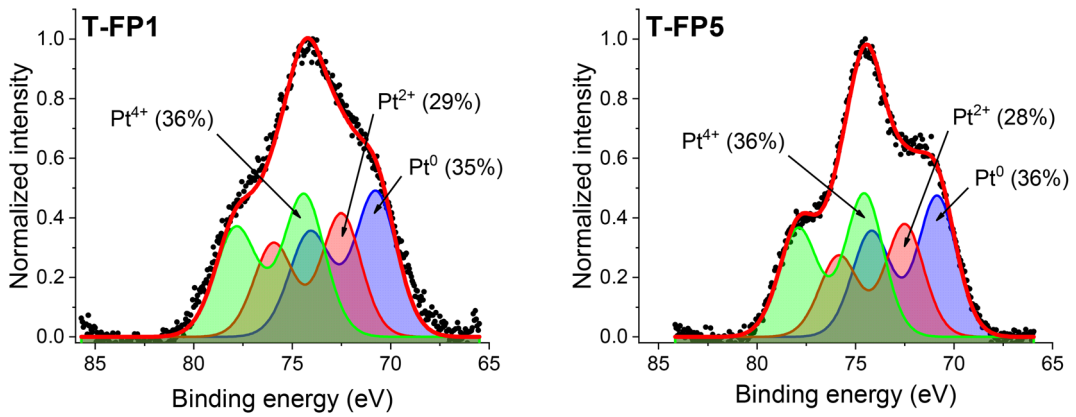

Fig. 4 Pt 4f-XPS spectra of samples T-FP1 (left) and T-FP5 (right).

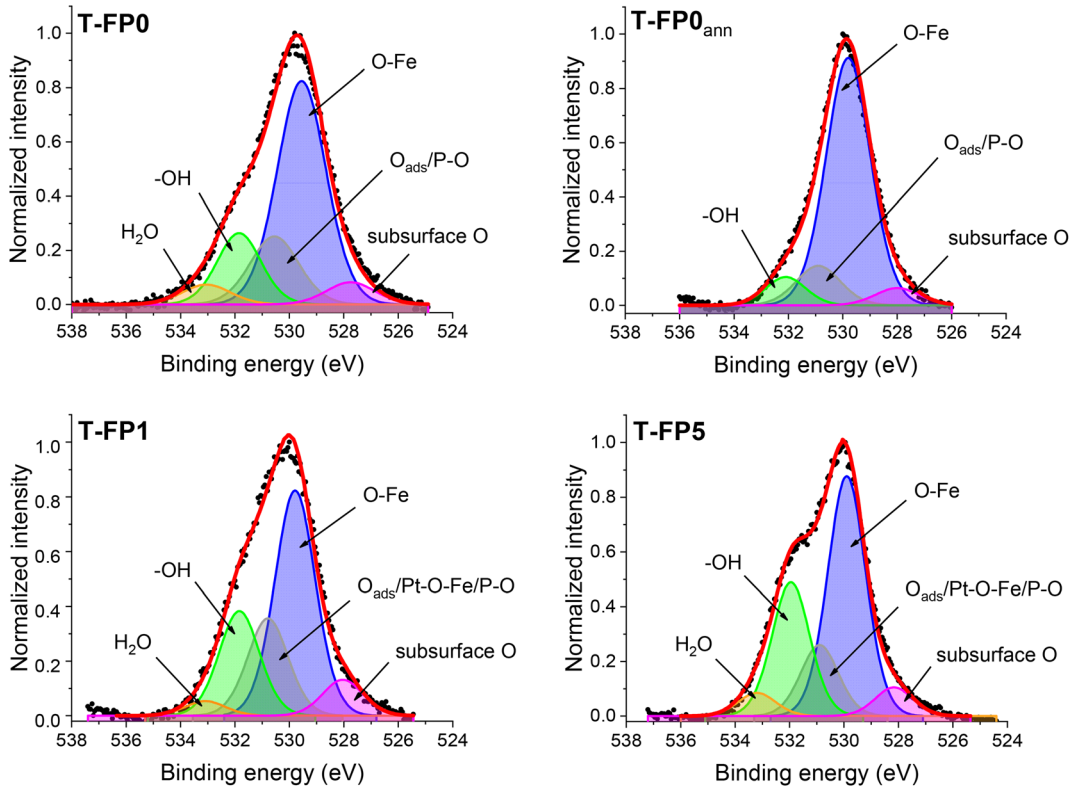

Fig. 5 O-1s-XPS spectra of synthesized samples.

formation, thereby increasing the density of active sites beneficial for catalytic and sensing activity.

3.4. TGA/DSC results

The thermal stability of the hematite sample (T-FP0) was investigated over a temperature range of 35–1000 °C using a thermogravimetric analyzer (TGA). Three distinct weight-loss stages are observed below 650 °C (Fig. S10, SI), corresponding to the removal of physisorbed and chemisorbed water, hydroxyl groups, and residual phosphate species, resulting in the formation of stable α-Fe_2O_3. The thermal stability of the sample above 650 °C confirms complete transformation into hematite.[50–52] The key temperatures used for gas sensing (363 K, 463 K and 553 K) and annealing (380 °C) are indicated for reference in Fig. S10 of the SI. Detailed TGA/DTG/DSC analysis is provided in Fig. S11 of the SI.

3.5. Mössbauer spectroscopy results

^{57}Fe Mössbauer spectroscopy was used to investigate the iron microenvironments in Pt-free hematite nanotubes (T-FP0) and Pt-decorated samples (T-FP1 and T-FP5). The room-temperature Mössbauer spectra in Fig. S12 of the SI display four sextet components (A–D), indicating multiple iron microenvironments with varying degrees of structural order. The corresponding hyperfine field distributions in Fig. S13 of the SI show a higher fraction of the well-ordered hematite component (A) in Pt-decorated samples.[53] The Mössbauer parameters obtained from these spectra are summarized in Table S4 of the SI. To confirm the stability of these microenvironments, T-FP1 was also analyzed at 150 K (Fig. S14, SI), revealing two distinct components – one corresponding to the weakly ferromagnetic state and another to the antiferromagnetic state – consistent with a partial recovery of the Morin transition. The associated fitting parameters are listed in Table S5.

Low-temperature Mössbauer spectra (87–88 K) in Fig. S15 of the SI further highlight clear differences between Pt-free and Pt-decorated samples. The Pt-free T-FP0 sample remained in the weakly ferromagnetic state, whereas T-FP1 and T-FP5 exhibited two distinct sextet components, confirming that part of the hematite phase had undergone the Morin transition. The low-temperature Mössbauer parameters are provided in Table S6 of the SI. These results indicate that Pt loading and the associated thermal treatment influence the magnetic ordering of hematite by promoting the formation of structurally more ordered domains with reduced strain and defect concentration, resulting in a more ideal crystalline phase.[16,19,54,55] Detailed Mössbauer spectra, fitting parameters, and hyperfine field distributions are provided in Sec. S2.5. of the SI.

3.6. Electron paramagnetic resonance spectroscopy results

X-band EPR spectroscopy was used to investigate the magnetic behavior of the samples between 150 and 290 K. Comparison of

the spectra at 150 and 290 K in Fig. S16 of the SI shows pronounced broadening and increased intensity for the Pt-decorated samples (T-FP1 and T-FP5) compared to the Pt-free T-FP0, indicating the formation of more magnetically ordered hematite domains after Pt decoration and heat treatment. The detailed temperature evolution of the EPR signal in Fig. S17 of the SI reveals a progressive decrease in signal intensity upon cooling, consistent with the suppression of the weak ferromagnetic resonance mode (LFWF) as the Morin transition occurs in Pt-decorated samples. The first integral of the EPR signals in Fig. S18 of the SI confirms that the center of the absorption band lies near zero magnetic field and that its intensity decreases with decreasing temperature, supporting the assignment of this resonance to the LFWF mode characteristic of the ideal hematite structure.[56–58]

The absence of a broad absorption feature around $g \approx 2$ excludes the presence of superparamagnetic particles, confirming the morphological and magnetic consistency of the samples. These results demonstrate that Pt loading and thermal treatment enhance magnetic ordering in hematite by reducing structural defects and modifying local magnetic anisotropy, in agreement with Mössbauer spectroscopy findings.[56] Detailed temperature-dependent EPR spectra and signal analyses are provided in Sec. S2.6 of the SI.

3.7. Results of magnetization measurements

Fig. 6 shows the temperature dependence of magnetization at $H = 100$ Oe, revealing the typical bifurcation between ZFC and FCC/FCW curves characteristic of small magnetic particles. The absence of a maximum in the ZFC curves indicates that magnetic moments remain blocked up to the highest measured temperatures, consistent with the high anisotropy energy barriers of the elongated hematite particles.

As shown in Fig. 6, only the annealed samples (T-FP0$_{ann}$ and T-FP5) exhibit the Morin transition in part of the samples, leading to the conclusion that the applied heat treatments are a crucial factor responsible for the recovery of the Morin transition. Heat treatment reduces crystal defects and internal strain and enhances crystal growth, which together promote the Morin transition. Differences in T_M and thermal hysteresis between the annealed samples are probably due to differences

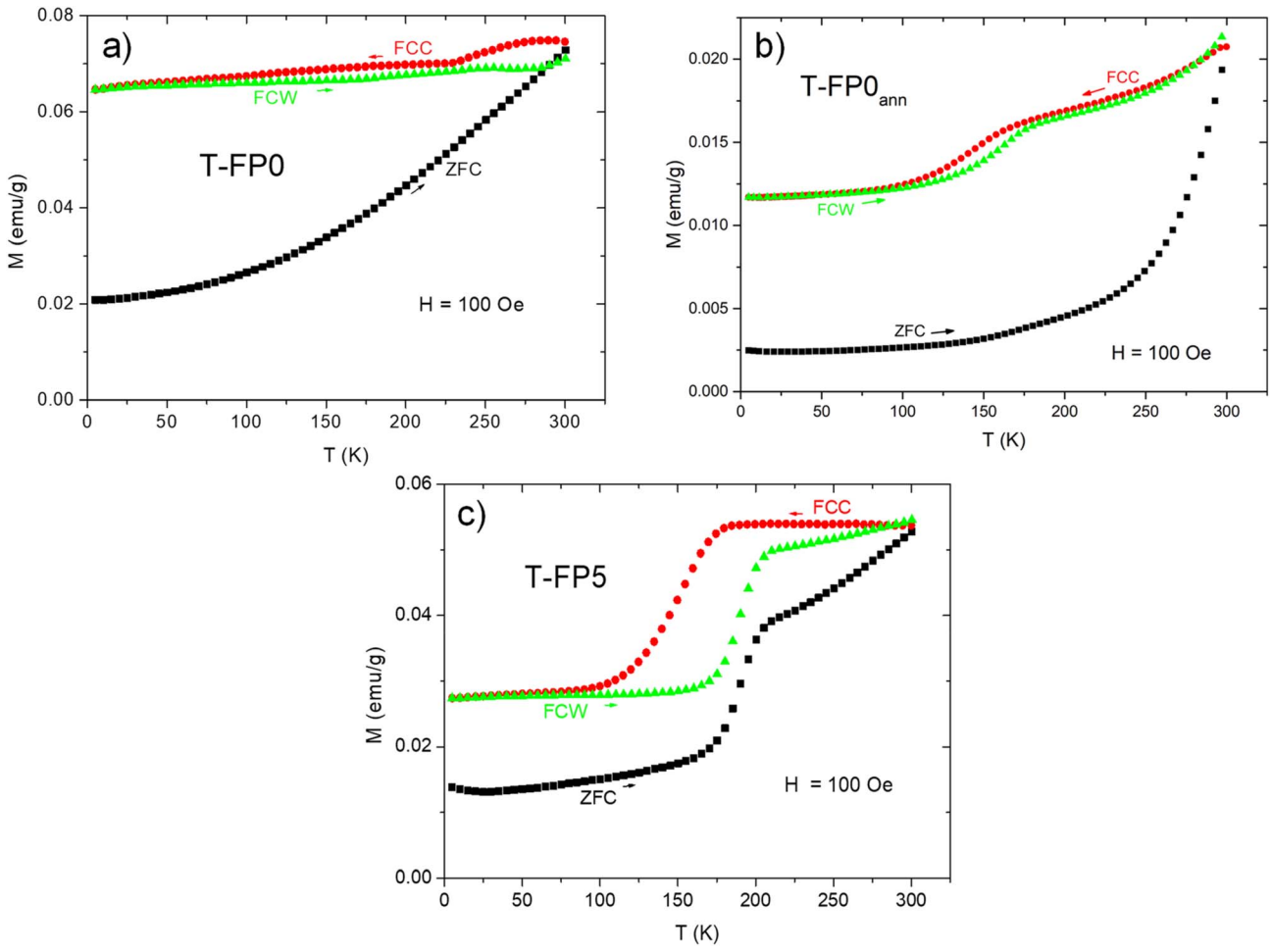

Fig. 6 Temperature dependence of magnetization for (a) T-FP0, (b) T-FP0$_{ann}$ and (c) T-FP5 measured at $H = 100$ Oe during warming after zero-field cooling (ZFC), followed by measurements during cooling in $H = 100$ Oe (FCC) and warming in $H = 100$ Oe (FCW).

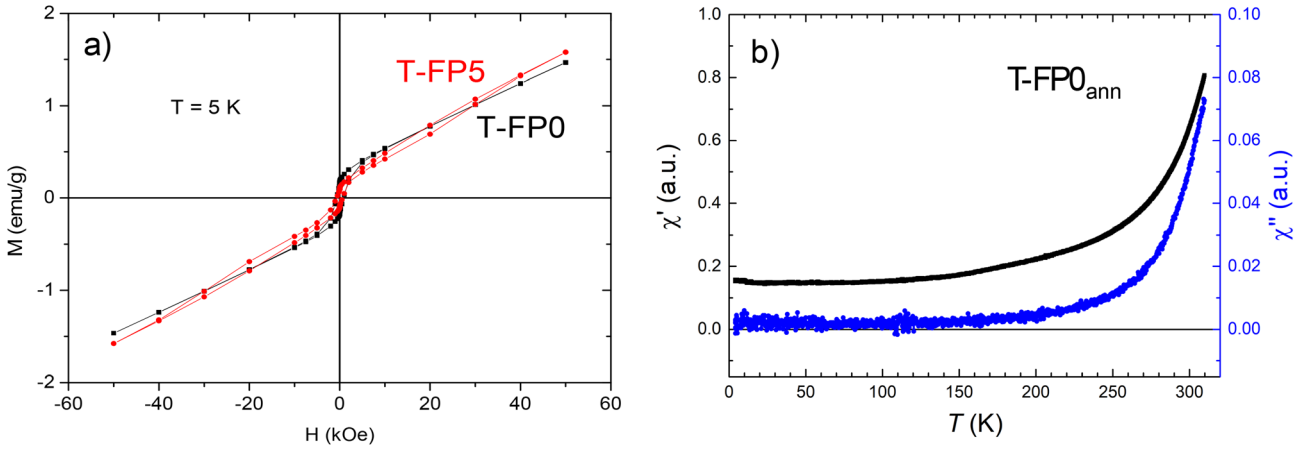

Fig. 7 (a) Magnetization as a function of magnetic field measured at $T = 5$ K for the T-FP0 and T-FP5 samples, (b) temperature dependence of ac magnetic susceptibility for the T-FP0$_{ann}$ sample measured with $H_{ac} = 3.2$ Oe and $f = 231$ Hz. Left axis (black): real part of ac susceptibility, right axis (blue): imaginary part of ac susceptibility.

in morphology, strain and impurities in these samples.[59] A more detailed discussion of the temperature-dependent magnetic behavior is provided in Sec. S2.7 of the SI.

The magnetic hysteresis curves measured at 5 K (Fig. 7a) confirm that both T-FP0 and T-FP5 display predominantly antiferromagnetic behavior with a minor ferromagnetic contribution, typical of weakly ferromagnetic hematite. The linear increase in magnetization at high fields indicates that antiferromagnetism is the dominant interaction, while the small hysteresis at low fields results from slow relaxation of weak ferromagnetic domains.

AC magnetic susceptibility measurements of T-FP0$_{ann}$ (Fig. 7b) show no distinct signature of the Morin transition, consistent with only a fraction of the material undergoing the transition. The gradual increase in both the real and imaginary components at higher temperatures reflects slow magnetic relaxation and high anisotropy barriers.[59] A detailed discussion and comparison with previously reported hematite nanostructures are provided in Sec. S2.7. of the SI.

3.8. Hydrogen gas sensing properties

The electrical resistance of the samples was measured at sequentially increasing H_2 concentrations at different temperatures in air and nitrogen. The resulting sensor responses ($\Delta R/R_0$) are plotted as a function of hydrogen concentration, covering the full range up to 400 ppm to illustrate the saturation effect. The average baseline resistance values (R_0) used for the response calculations are shown in Table S7 of the SI. Error bars represent the standard deviation of three repeated measurements, confirming the reproducibility of the results and indicating occasional signal noise or sensor drift.

3.8.1. Effect of Pt decoration and temperature on hydrogen sensing in air. Gas sensing with hematite-based materials relies primarily on the adsorption of oxygen and its subsequent interaction with target gases such as hydrogen. In ambient air, oxygen molecules are adsorbed and ionized (O_2^-, O^-, and O^{2-}) on the sensor surface, capturing free electrons from the hematite conduction band and forming a surface depletion layer, which increases resistance. When the sensor is exposed to hydrogen gas, the adsorbed oxygen reacts with hydrogen molecules, releasing electrons back into the conduction band, reducing the electron depletion width and lowering the electrical resistance. This principle underlies the sensitivity of n-type semiconductor materials such as hematite, as discussed in Liu *et al.*[60] and Goel *et al.*[61] and has also been proposed in other related studies, including Wang *et al.*[62] and Guo *et al.*[37] A schematic illustration of this sensing mechanism is shown in Fig. S19 of the SI. Similar mechanistic schemes for n-type metal oxide semiconductors exposed to reducing gases have been reported in previous studies, including Goel *et al.*,[61] Shrisha *et al.*,[27] Wang *et al.*[63] and Merah *et al.*[64]

Fig. 8 summarizes the hydrogen sensing behavior of all samples at 363 K, 463 K and 553 K. Pt-decorated hematite samples consistently exhibit much stronger responses than Pt-free hematite, both annealed and unannealed. At 363 K, Pt-free hematite samples show no measurable sensor response, likely because adsorbed water molecules block the active sites, as shown by TGA analysis in Fig. S10 of the SI). In contrast, the presence of Pt markedly enhances hydrogen detection at lower temperatures, confirming its key catalytic role. Notably, a measurable response for Pt-decorated samples was also observed at room temperature. However, signal instability and baseline drift prevented reliable quantitative analysis. This nevertheless indicates that the sensing mechanism remains active even at low temperatures, underscoring the catalytic efficiency of Pt sites. As reviewed by Goel *et al.*, noble metal decoration enhances gas sensing through catalytic hydrogen

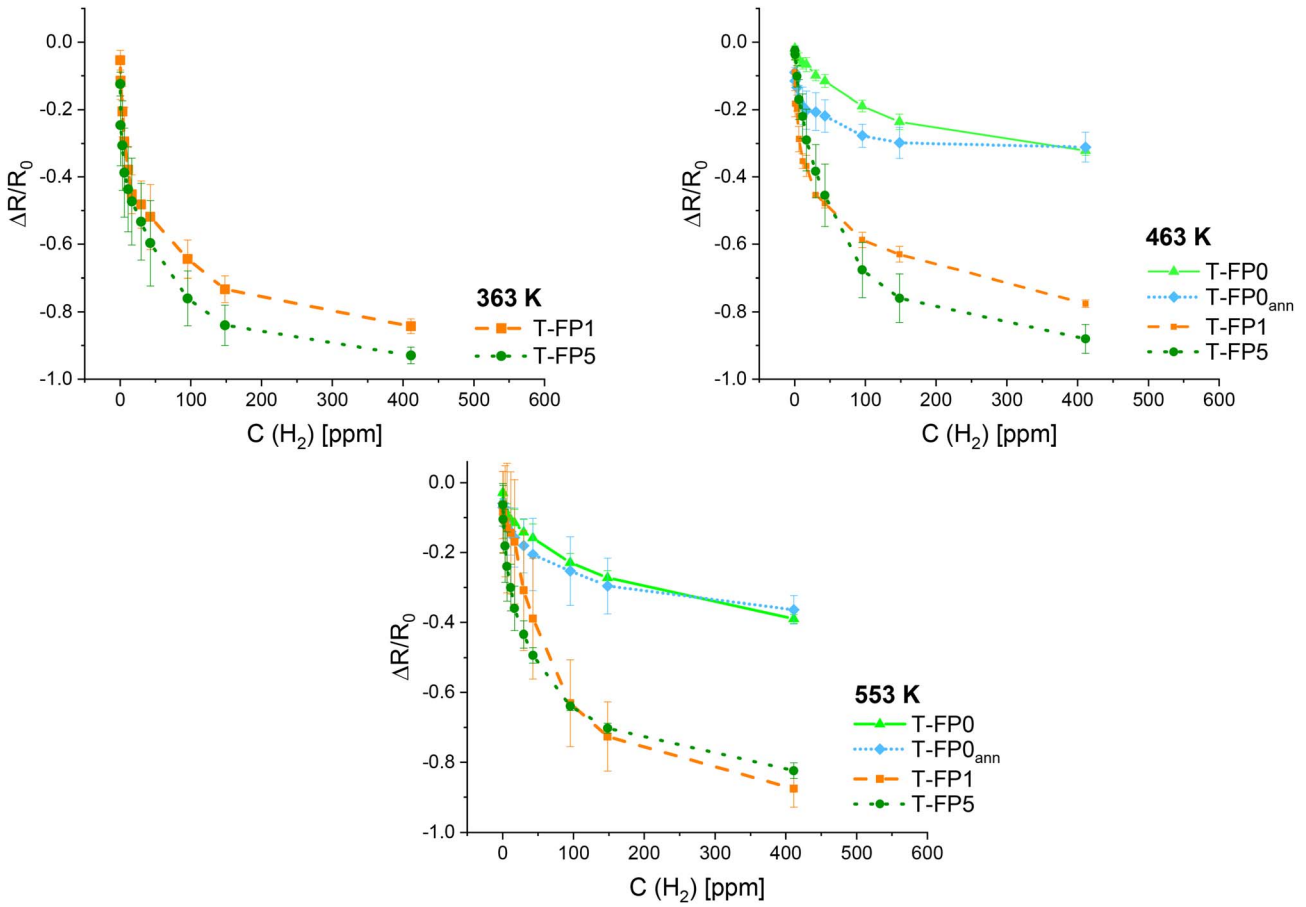

Fig. 8 Hydrogen gas sensing responses of Pt-free (T-FP0 (green triangle) and T-FP0$_{ann}$ (blue diamond)) and Pt-decorated hematite samples (T-FP1 (orange square) and T-FP5 (green circle)) as a function of H_2 concentration at 363 K, 463 K and 553 K in air. The error bars represent the propagated uncertainties in the response, calculated from the standard deviations of R and R_0, and their covariance.

dissociation, hydrogen spillover and the formation of active sites that facilitate gas interactions, while also lowering the activation energy required for gas reactions and improving sensitivity and selectivity.[61] Similar mechanisms have also been discussed by Zhu *et al.* and Shah *et al.*[65,66]

Although Pt-free samples exhibit nearly identical sensitivity across the full concentration range (Fig. 8), their LOD values determined at 463 K show a slight difference: 3.5 ppm for T-FP0 and 2.0 ppm for the annealed T-FP0$_{ann}$, without affecting the overall interpretation, as their response slopes remain similar. In contrast, Pt-decorated samples display notably improved performance, with LOD values of 1.1 ppm for T-FP1 and 1.0 ppm for T-FP5, demonstrating the effectiveness of Pt modification in enhancing hydrogen sensitivity.[67] Consistent with Fig. 8, the sensitivities of T-FP1 and T-FP5 are very similar (with a slight advantage for 5 mol% Pt over the full range), while their LOD values are practically identical. These results indicate that even a small amount of platinum ($\approx$1 mol%) is sufficient to substantially improve sensor efficiency. The optimal operating temperature was determined to be 463 K, providing strong sensor performance at a relatively low temperature, which is advantageous for practical hydrogen sensing applications. At this temperature, ionized oxygen species (primarily O^-) are stable and active on n-type metal oxide surfaces, enabling effective modulation of the surface depletion layer during hydrogen sensing, as reported in the literature.[24] A comparative overview of hydrogen sensing performance reported for various MOS-based sensors is provided in Table S8 of the SI.

The sensor response time decreased as temperature increased for all samples, indicating faster kinetics at higher operating temperatures. Fig. S20 in the SI shows the average sensor response times for various sample series at different temperatures. Samples T-FP0 and T-FP0$_{ann}$ showed no measurable response at 363 K, suggesting that higher temperatures are needed to activate their sensing properties. In contrast, T-FP1 and T-FP5 responded at all tested temperatures (363 K, 463 K and 553 K), with response times decreasing significantly at higher temperatures. Of the temperatures

tested, 463 K was identified as the optimal operating temperature, with response times of 3.6 s for T-FP1 and 8.3 s for T-FP5. This temperature dependence is attributed to faster adsorption and desorption kinetics and enhanced gas–surface interactions at higher temperatures, consistent with trends commonly reported for metal oxide gas sensors.[60,62] Within the humidity range of 20–40%, the sensor parameters (sensitivity, LOD, response time, and recovery time) remained stable over repeated cycles and during long-term testing.

Comparison with previously reported irregular hematite nanoparticles synthesized by planetary ball milling[4] in Fig. S21 and S22 of the SI confirms that only Pt-decorated samples exhibited measurable hydrogen responses, highlighting the critical role of morphology and synthesis method. Hydrothermally synthesized Pt-decorated nanotubes achieved a much lower LOD (1 ppm compared to 8 ppm for irregular particles), attributed to their higher surface area and improved gas diffusion. As shown in Fig. S23 of the SI, both Pt decoration and controlled nanotube morphology significantly increased the specific surface area, thereby enhancing charge transfer and catalytic activity, consistent with previously reported trends for morphology-tailored metal oxide sensors.[37,60–62,67]

3.8.2. Influence of measurement atmosphere: comparison between air and N_2. To gain a deeper understanding of the sensor behavior of the prepared samples and to evaluate the influence of the ambient atmosphere, additional measurements were conducted in nitrogen (N_2). Comparing the responses in air and N_2 isolates the role of adsorbed oxygen in the sensing mechanism and highlights the catalytic contribution of platinum under inert conditions. For both Pt-decorated samples, sensitivity increased with temperature in both atmospheres, but overall responses were higher in N_2 across the entire concentration range, emphasizing the influence of the ambient gases. The response plots for both samples at each temperature are shown in Fig. 9 and 10. This trend is consistent with previous findings, which show that competitive adsorption between oxygen and target gases can reduce sensor performance.[68,69] In nitrogen, where oxygen is absent, hydrogen molecules can more easily adsorb and dissociate on Pt, enhancing the spillover effect, increasing electron return to hematite, reducing the electron depletion width, and leading to

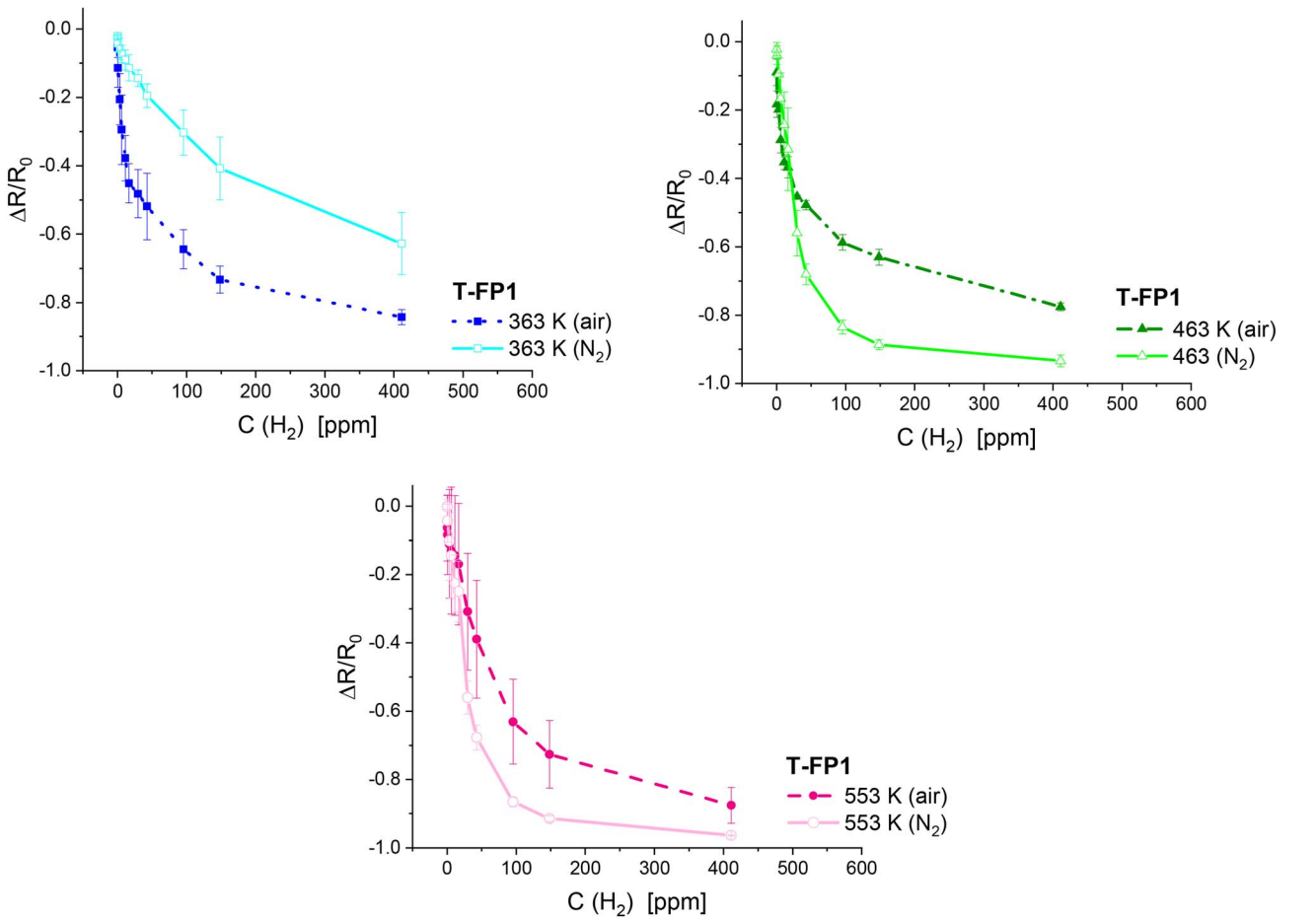

Fig. 9 Comparison of the response of the T-FP1 sample to hydrogen gas, measured in air and nitrogen atmospheres at 363 K, 463 K and 553 K, with separate graphs for each temperature. The error bars represent the propagated uncertainties in the response, calculated from the standard deviations of R and R_0, and their covariance.

higher overall responses. A schematic comparison of the proposed sensing mechanisms in air and nitrogen atmospheres is shown in Fig. 11.

Although the general sensor response was higher in nitrogen, this difference is only partially reflected in the LOD values. At 463 K, a noticeable LOD improvement was observed for T-FP5 (0.3 ppm in N_2 *vs.* 1.0 ppm in air), whereas the LOD values for Pt-free hematite and T-FP1 remained nearly unchanged. This suggests that LOD alone does not fully represent sensor performance and that complete response curves provide additional insight. The higher Pt loading in T-FP5 likely facilitates more efficient hydrogen dissociation and sensing under inert conditions, while the lower catalytic activity of Pt-free and moderately Pt-decorated samples limits their response. Although the LOD values for T-FP1 are comparable in both atmospheres, the overall sensitivity is higher in nitrogen, particularly at higher concentrations. These findings confirm that Pt-decorated samples generally show enhanced performance in nitrogen due to the absence of oxygen competition and a more pronounced spillover effect on Pt.

In contrast, Pt-free hematite samples (T-FP0 and T-$FP0_{ann}$) show markedly different sensing behavior in nitrogen compared to Pt-decorated samples (Fig. S24 and S25, SI). Both Pt-free samples show no measurable response to hydrogen at 363 K, consistent with their behavior in air, while T-FP0 displays an unusual increase in resistance at 463 K (Fig. S24, SI), likely due to the desorption of surface water and hydroxyl groups, which expands the electron depletion width and increases resistance. At higher temperatures, both samples exhibit the expected n-type response, with resistance decreasing upon hydrogen exposure. Although their LOD values remain similar in air and nitrogen, the overall sensor response is more pronounced in nitrogen across the entire concentration range. In the absence of Pt, which catalyzes H_2 dissociation and stabilizes sensor behavior, Pt-free hematite is more sensitive to surface chemical changes, resulting in less stable and less efficient hydrogen detection.

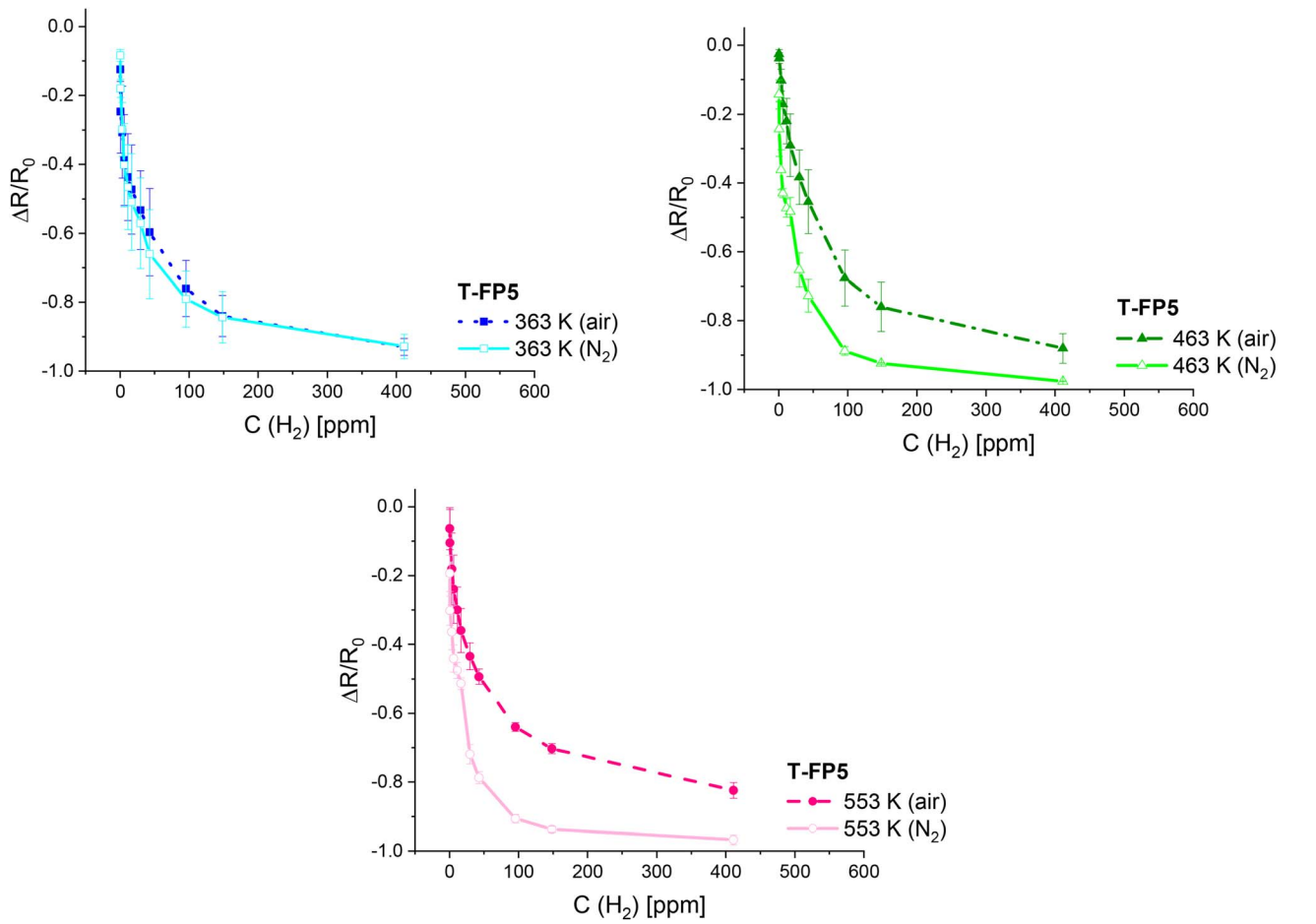

Fig. 10 Comparison of the response of the T-FP5 sample to hydrogen gas, measured in air and nitrogen atmospheres at 363 K, 463 K and 553 K, with separate graphs for each temperature. The error bars represent the propagated uncertainties in the response, calculated from the standard deviations of R and R_0, and their covariance.

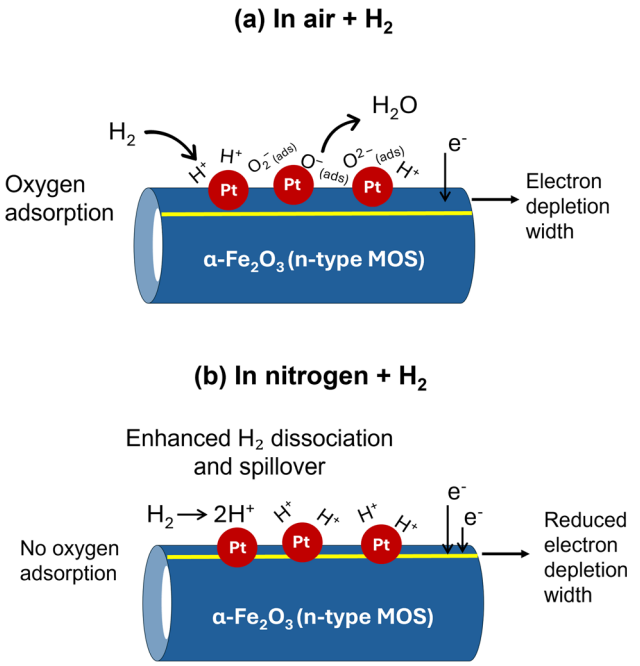

Fig. 11 Schematic illustration of the proposed hydrogen sensing mechanism of Pt-decorated α-Fe_2O_3 in (a) air and (b) nitrogen atmospheres, showing enhanced H_2 dissociation and spillover in the absence of oxygen and the resulting reduced electron depletion width in N_2.

4 Conclusions

Hydrothermal synthesis in the presence of phosphate produces α-Fe_2O_3 nanotubes with a highly hydrated and hydroxylated surface, which strongly influences their magnetic and sensing behavior. The Pt-free material lacks the Morin transition, indicating significant lattice disorder caused by surface hydration. Thermal treatment combined with Pt decoration partially restores magnetic ordering, showing that Pt loading reduces strain and defect concentration and promotes the formation of more structurally ordered hematite domains. These results demonstrate that controlled Pt decoration is an effective method for tuning the structural, magnetic and electronic properties of α-Fe_2O_3 nanotubes for hydrogen sensing. Notably, only 1 mol% Pt is sufficient to achieve rapid, low-ppm hydrogen detection at moderate temperatures. The consistently higher responses in nitrogen highlight the limiting effect of oxygen competition in air and confirm the role of Pt in promoting hydrogen spillover and accelerating surface reaction kinetics. Unlike previous studies that mainly report sensing performance, this work demonstrates how magnetic and microstructural ordering induced by Pt decoration directly influences hydrogen sensing behavior.

Overall, the strong synergy between nanotubular morphology and Pt decoration yields stable, highly responsive and low-temperature operable α-Fe_2O_3 sensors. These findings clarify how structure affects performance and indicate that further improvements can be achieved through morphology control and precise optimization of noble-metal decoration.

Author contributions

M. Šoltić: investigation, formal analysis, validation, data curation, visualization, writing – original draft, writing – review & editing, M. Gracheva: investigation, visualization, writing – review & editing, N. Baran: methodology, supervision, G. Dražić: investigation, R. Peter: investigation, validation, K. Lázár: validation, G. Štefanić: investigation, M. Marciuš: investigation, N. Novosel: investigation, visualization, L. Ferenc Kiss: validation, M. A. van Spronsen: investigation, validation, M. Ivanda: resources, Z. Klencsár: investigation, visualization, writing – review & editing, funding acquisition, M. Gotić: conceptualization, funding acquisition, supervision, project administration, validation, methodology, writing – review & editing.

Conflicts of interest

The authors declare no conflicts of interest.

Data availability

All data supporting the findings of this study are available in the article and its supplementary information (SI). Supplementary information: additional figures and graphs, extended discussion and explanations, further measurements, and detailed methodological information on the applied characterisation techniques. See DOI: https://doi.org/10.1039/d5ra08865h.

Acknowledgements

This work was financially supported by the Hungarian National Research, Development, and Innovation Office (NKFIH), grant number 2019–2.1.11-TÉT-2020-00221, and the Croatian Science Foundation under the project IP-2019-04–1195 "Platinum decorated iron tin oxide solid solutions for hydrogen gas sensing" (HydGasSens). The authors would also like to acknowledge the support of the Centre of Excellence for Advanced Materials and Sensing Devices (CEMS, http://cems.irb.hr) and thank Dr Ivan Marić (Ruđer Bošković Institute) for his valuable comments, critical reading and insightful discussions during the preparation of the manuscript, as well as Fabio Faraguna and Rafael Anelić (Faculty of Chemical Engineering and Technology, Zagreb) for their valuable assistance in recording the DSC, TGA and DTA measurements. We acknowledge Diamond Light Source for time on Beamline B07c under Proposal cm-40615. Finally, Z.K. expresses thanks to Prof. Ferenc Simon (Institute of Physics, Budapest University of Technology and Economics, Budapest, Hungary) for making available the applied spectrometer for recording the EPR spectra. N.N. acknowledges the support of the projects: Ground states in competition–strong correlations, frustration and disorder (FrustKor) financed by the Croatian Government and the European Union through the National Recovery and Resilience Plan 2021–2026 (NPOO) and Cryogenic Centre at the Institute of Physics (KaCIF) co-financed by the Croatian Government and the European Union through

the European Regional Development Fund-Competitiveness and Cohesion Operational Programme (Grant No. KK.01.1.1.02.0012).

References

1 I. Marić, G. Dražić, E. Radin, R. Peter, M. Škrabić, T. Jurkin, A. Pustak, N. Baran, L. Mikac, M. Ivanda, M. Petravić, G. Štefanić and M. Gotić, Impact of platinum loading and dispersion on the catalytic activity of Pt/SnO_2 and Pt/α-Fe_2O_3, *Appl. Surf. Sci.*, 2023, **607**, 155073.

2 Z. A. Che Ramli, J. Pasupuleti, A. Mohd Zainoodin, N. F. H. Nik Zaiman, K. N. Ahmad, N. F. Raduwan, Y. N. Yusoff, W. N. R. Wan Isahak, T. S. Tengku Saharuddin and T. K. Sieh, Unlocking the potential of Pt-based and metal oxides catalysts in liquid fuel cells technologies: Performance and challenges, *Ain Shams Eng. J.*, 2024, **15**, 103112.

3 C.-H. Cui and S.-H. Yu, Engineering interface and surface of noble metal nanoparticle nanotubes toward enhanced catalytic activity for fuel cell applications, *Acc. Chem. Res.*, 2013, **46**, 1427–1437.

4 M. Šoltić, Z. Klencsár, G. Dražić, M. Gotić, M. Ivanda and N. Baran, Hydrogen gas sensing properties of mechanochemically dispersed platinum on α-Fe_2O_3 support, *Sens. Actuators, A*, 2024, **376**, 115539.

5 G. K. Pradhan and K. M. Parida, Fabrication, growth mechanism, and characterization of α-Fe_2O_3 nanorods, *ACS Appl. Mater. Interfaces*, 2011, **3**, 317–323.

6 E. Radin, G. Štefanić, G. Dražić, I. Marić, T. Jurkin, A. Pustak, N. Baran, M. Raić and M. Gotić, Solid-state dispersions of platinum in the SnO_2 and Fe_2O_3 nanomaterials, *J. Nanomater.*, 2021, **11**, 3349.

7 C. Wu, P. Yin, X. Zhu, C. OuYang and Y. Xie, Synthesis of hematite (α-Fe_2O_3) nanorods: Diameter-size and shape effects on their applications in magnetism, lithium ion battery, and gas sensors, *J. Phys. Chem. B*, 2006, **110**, 17806–17812.

8 N. Arif, M. N. Zafar, M. Batool, M. Humayun, M. A. Iqbal, M. Younis, L. Li, K. Li and Y. J. Zeng, Recent advances and perspectives on iron-based photocatalysts, *J. Mater. Chem. C*, 2024, **12**, 12653–12691.

9 R. Lang, W. Xi, J.-C. Liu, Y.-T. Cui, T. Li, A. F. Lee, F. Chen, Y. Chen, L. Li, L. Li, J. Lin, S. Miao, X. Liu, A.-Q. Wang, X. Wang, J. Luo, B. Qiao, J. Li and T. Zhang, Non defect-stabilized thermally stable single-atom catalyst, *Nat. Commun.*, 2019, **10**, 234.

10 H. Liu, K. Tian, J. Ning, Y. Zhong, Z. Zhang and Y. Hu, One-Step Solvothermal Formation of Pt Nanoparticles Decorated Pt^{2+}-doped α-Fe_2O_3 Nanoplates with Enhanced Photocatalytic O_2 Evolution, *ACS Catal.*, 2019, **9**, 1211–1219.

11 C.-J. Jia, L.-D. Sun, Z.-G. Yan, L.-P. You, F. Luo, X.-D. Han, Y.-C. Pang, Z. Zhang and C.-H. Yan, Single-Crystalline Iron Oxide Nanotubes, *Angew. Chem.*, 2005, **117**, 4402–4407.

12 H.-J. Kim, K.-I. Choi, A. Pan, I.-D. Kim, H.-R. Kim, K.-M. Kim, C. W. Na, G. Cao and J.-H. Lee, Template-free solvothermal synthesis of hollow hematite spheres and their applications in gas sensors and Li-ion batteries, *J. Mater. Chem.*, 2011, **21**, 6549–6555.

13 X. Hu, J. C. Yu, J. Gong, Q. Li and G. Li, α-Fe2O3 nanorings prepared by a microwave-assisted hydrothermal process and their sensing properties, *Adv. Mater.*, 2007, **19**, 2324–2329.

14 F. Zhang, H. Yang, X. Xie, L. Li, L. Zhang, J. Yu, H. Zhao and B. Liu, Controlled synthesis and gas-sensing properties of hollow sea urchin-like α-Fe_2O_3 nanostructures and α-Fe_2O_3 nanocubes, *Sens. Actuators B Chem.*, 2009, **141**, 381–389.

15 G. Dražić, G. Štefanić, T. Jurkin and M. Gotić, Impact of cadmium and phosphate ions on the hematite nanorings formation, *J. Mol. Struct.*, 2017, **1140**, 113–121.

16 F. J. Morin, Magnetic Susceptibility of α-Fe_2O_3 and α-Fe_2O_3 with Added Titanium, *Phys. Rev.*, 1950, **78**, 819–820.

17 Ö. Özdemir, D. J. Dunlop and T. S. Berquó, Morin transition in hematite: Size dependence and thermal hysteresis, *Geochem., Geophys., Geosyst.*, 2008, **9**, Q10Z01.

18 D. Kubániová, L. Kubíčková, T. Kmječ, K. Závěta, D. Nižňanský, P. Brázda, M. Klementová and J. Kohout, Hematite: Morin temperature of nanoparticles with different size, *J. Magn. Magn. Mater.*, 2019, **475**, 611–619.

19 M.-Z. Dang, D. G. Rancourt, J. E. Dutrizac, G. Lamarche and R. Provencher, Interplay of surface conditions, particle size, stoichiometry, cell parameters, and magnetism in synthetic hematite-like materials, *Hyperfine Interact.*, 1998, **117**, 271–319.

20 P. Tartaj, T. González-Carreño and C. J. Serna, From Hollow to Dense Spheres: Control of Dipolar Interactions by Tailoring the Architecture in Colloidal Aggregates of Superparamagnetic Iron Oxide Nanocrystals, *Adv. Mater.*, 2004, **16**, 529–533.

21 K. Woo, H. J. Lee, J.-P. Ahn and Y. S. Park, Sol-Gel Mediated Synthesis of Fe_2O_3 Nanorods, *Adv. Mater.*, 2003, **15**, 1761–1764.

22 S. J. Park, S. Kim, S. Lee, Z. G. Khim, K. Char and T. Hyeon, Synthesis and magnetic studies of uniform iron nanorods and nanospheres, *J. Am. Chem. Soc.*, 2000, **122**, 8581–8582.

23 A. Mirzaei, B. Hashemi and K. Janghorban, α-Fe2O3 based nanomaterials as gas sensors, *J. Mater. Sci.: Mater. Electron.*, 2016, **27**, 3109–3144.

24 Z. Li, Z. J. Yao, A. A. Haidry, T. Plecenik, L. J. Xie, L. C. Sun and Q. Fatima, Resistive-type hydrogen gas sensor based on TiO_2: A review, *Int. J. Hydrogen Energy*, 2018, **43**, 21114–21132.

25 N. K. Maksimova, E. Y. Sevastyanov, E. V. Chernikov, P. M. Korusenko, S. N. Nesov, S. V. Kim, A. A. Biryukov, N. V. Sergeychenko, N. A. Davletkildeev and D. V. Sokolov, Sensors based on tin dioxide thin films for the detection of pre-explosive hydrogen concentrations, *Sens. Actuators B Chem.*, 2021, **341**, 130020.

26 V. T. Duoc, H. Nguyen, T. M. Ngoc, C. T. Xuan, C. M. Hung, N. Van Duy and N. D. Hoa, Hydrogen gas sensor based on self-heating effect of SnO_2/Pt thin film with ultralow power consumption, *Int. J. Hydrogen Energy*, 2024, **61**, 774–782.

27 C.-M. Shrisha, K. G. Wu, G.-Y. Motora, D.-H. Chen and N. S. Kuo, Gultom, Highly efficient reduced tungsten

oxide-based hydrogen gas sensor at room temperature, *Mater. Sci. Eng. B*, 2023, **289**, 116285.

28 R. Barathy, P. V. K. Yadav, A. Mondal, K. Ramakrishnan, J. Jarugala, C. Liu and Y. A. K. Reddy, Enhanced response of WO_3 thin film through Ag loading towards room temperature hydrogen gas sensor, *Chemosphere*, 2024, **353**, 141545.

29 M. Patrnčiak and M. Vidiš, Ľ. Staňo, I. Shpetnyy, T. Roch, B. Grančič, L. Satrapinskyy, P. Ďurina, M. Mikula, T. Plecenik, Highly sensitive hydrogen gas sensor based on a capacitor-like Pt/TiO_2/Pt structure with large-scale nanoporous top electrode, *Int. J. Hydrogen Energy*, 2025, **99**, 137–145.

30 Y. Yao, H. Sun, C. Cao, R. Yang, Z. Yan, Y. Deng, S. Liu, Q. Xu and Y. Qin, Pd nanoislands-modified ZnO nanowire-network for sensitive and linear hydrogen sensing, *Nano Energy*, 2025, **133**, 110512.

31 M. Muhajir, P. Puspitasari and J. A. Razak, Synthesis and Applications of Hematite α-Fe_2O_3 : a Review, *J. Mech. Eng. Sci. Technol.*, 2019, **3**, 51–58.

32 L. Gao, Y. Tian, A. Hussain, Y. Guan and G. Xu, Recent developments and challenges in resistance-based hydrogen gas sensors based on metal oxide semiconductors, *Anal. Bioanal. Chem.*, 2024, **416**, 3697–3715.

33 R. Guan, T. Ai, J. Zhang, J. Li, Y. Zhang, Y. Yin and J. Lu, High-performance hydrogen sensor based on γ-Fe_2O_3/α-Fe_2O_3 heterostructures produced by a one-step hydrothermal method, *Int. J. Hydrogen Energy*, 2024, **86**, 968–975.

34 G. Jiao, P. Jia, Y. Zhang, H. Zhang, J. Zhai, Z. Ding and D. Zhang, Construction of high-performance Fe_2O_3-In_2O_3 heterostructure-based hydrogen gas sensor: Experimental and DFT calculation, *J. Alloys Compd.*, 2025, **1026**, 180378.

35 Y. Nakatani and M. Matsuoka, Effects of Sulfate Ion on Gas Sensitive Properties of α-Fe_2O_3 Ceramics, *Jpn. J. Appl. Phys.*, 1982, **21**, L758–L760.

36 T. Maosong, D. Guorui and G. Dingsan, Surface modification of oxide thin film and its gas-sensing properties, *Appl. Surf. Sci.*, 2001, **171**, 226–230.

37 L. Guo, N. Xie, C. Wang, X. Kou, M. Ding, H. Zhang, Y. Sun, H. Song, Y. Wang and G. Lu, Enhanced hydrogen sulfide sensing properties of Pt-functionalized α-Fe_2O_3 nanowires prepared by one-step electrospinning, *Sens. Actuators B Chem.*, 2018, **255**, 1015–1023.

38 N. Baran, H. Gebavi, L. Mikac, D. Ristić, M. Gotić, K. A. Syed and M. Ivanda, Sensing properties of oxidized nanostructured silicon surface on vaporized molecules, *Sensors*, 2019, **19**, 119.

39 S. Zhang, X. Chang, L. Zhou, X. Liu and J. Zhang, Stabilizing Single-Atom Pt on Fe_2O_3 Nanosheets by Constructing Oxygen Vacancies for Ultrafast H_2 Sensing, *ACS Sens.*, 2024, **9**, 2101–2109.

40 Y. M. Kwon, Y. Son, D. H. Lee, M. H. Lim, J. K. Han, M. Jang, S. Park, S. Kang, S. Yim, S. Myung, J. Lim, S. S. Lee, G. Bae, S.-H. Kim and W. Song, Enhancing selectivity and sensitivity in gas sensors through noble metal-decorated ZnO and machine learning, *Appl. Surf. Sci.*, 2025, **693**, 162750.

41 G. Pandey, M. Bhardwaj, S. Kumar, S. D. Lawaniya, M. Kumar, P. K. Dwivedi and K. Awasthi, Synergistic effects of Pd-Ag decoration on SnO/SnO_2 nanosheets for enhanced hydrogen sensing, *Sens. Actuators B Chem.*, 2024, **402**, 135062.

42 L. B. Tasyurek, E. Isik, I. Isik and N. Kilinc, Enhancing the performance of TiO_2 nanotube-based hydrogen sensors through crystal structure and metal electrode, *Int. J. Hydrogen Energy*, 2024, **54**, 678–690.

43 N. Baran, *PhD thesis*, University of Zagreb, 2022.

44 A. P. Grosvenor, B. A. Kobe, M. C. Biesinger and N. S. McIntyre, Investigation of multiplet splitting of Fe 2p XPS spectra and bonding in iron compounds, *Surf. Interface Anal.*, 2004, **36**, 1564–1574.

45 J.-C. Wang, J. Ren, H.-C. Yao, L. Zhang, J.-S. Wang, S.-Q. Zang, L.-F. Han and Z.-J. Li, Synergistic photocatalysis of Cr(VI) reduction and 4-Chlorophenol degradation over hydroxylated α-Fe_2O_3 under visible light irradiation, *J. Hazard. Mater.*, 2016, **311**, 11–19.

46 M. C. Biesinger, B. P. Payne, A. P. Grosvenor, L. W. M. Lau, A. R. Gerson and R. S. C. Smart, Resolving surface chemical states in XPS analysis of first row transition metals, oxides and hydroxides: Cr, Mn, Fe, Co and Ni, *Appl. Surf. Sci.*, 2011, **257**, 2717–2730.

47 F. Jiménez-Villacorta, C. Prieto, Y. Huttel, N. D. Telling and G. Van Der Laan, X-ray magnetic circular dichroism study of the blocking process in nanostructured iron-iron oxide core-shell systems, *Phys. Rev. B*, 2011, **84**, 172404.

48 X.-F. Lu, X.-Y. Chen, W. Zhou, Y.-X. Tong and G.-R. Li, α-Fe2O3@PANI core-shell nanowire arrays as negative electrodes for asymmetric supercapacitors, *ACS Appl. Mater. Interfaces.*, 2015, **7**, 14843–14850.

49 M. Chen, H. Yin, X. Li, Y. Qiu, G. Cao, J. Wang, X. Yang and P. Wang, Facet- and defect-engineered Pt/Fe2O3 nanocomposite catalyst for catalytic oxidation of airborne formaldehyde under ambient conditions, *J. Hazard. Mater.*, 2020, **395**, 122628.

50 M. Lin, L. Tng, T. Lim, M. Choo, J. Zhang, H. R. Tan and S. Bai, Hydrothermal Synthesis of Octadecahedral Hematite (α-Fe_2O_3) Nanoparticles: An Epitaxial Growth from Goethite (α-FeOOH), *J. Phys. Chem. C*, 2014, **118**, 10903–10910.

51 A. Rufus, N. Sreeju and D. Philip, Synthesis of biogenic hematite (α-Fe_2O_3) nanoparticles for antibacterial and nanofluid applications, *RSC Adv.*, 2016, **6**, 94206–94217.

52 A. A. Qureshi, S. Javed, H. M. A. Javed, M. Jamshaid, U. Ali and M. A. Akram, Systematic Investigation of Structural, Morphological, Thermal, Optoelectronic, and Magnetic Properties of High-Purity Hematite/Magnetite Nanoparticles for Optoelectronics, *J. Nanomater.*, 2022, **12**, 1635.

53 R. Zboril, M. Mashlan and D. Petridis, Iron(III) oxides from thermal processes-synthesis, structural and magnetic properties, Mössbauer spectroscopy characterization, and applications, *Chem. Mag.*, 2002, **14**, 969–982.

54 F. van der Woude, Mössbauer Effect in α-Fe_2O_3, *Phys. Status Solidi B*, 1966, **17**, 417–432.

55 T. Ruskov, T. Tomov and S. Georgiev, Mössbauer investigation of the Morin transition in hematite, *Phys. Status Solidi B*, 1976, **37**, 295–302.
56 C. Carbone, F. Di Benedetto, C. Sangregorio, P. Marescotti, L. A. Pardi and L. Sorace, Multifrequency EMR and magnetic characterization of synthetic powdered hematite, *J. Phys. Chem. C*, 2008, **112**, 9988–9995.
57 H. Kumagai, H. Abe, K. Ôno, I. Hayashi, J. Shimada and K. Iwanaga, Frequency dependence of magnetic resonance in α-Fe_2O_3, *Phys. Rev.*, 1955, **99**, 1116–1118.
58 P. W. Anderson, F. R. Merritt, J. P. Remeika and W. A. Yager, Magnetic resonance in α-Fe_2O_3, *Phys. Rev.*, 1954, **93**, 717–718.
59 M. Vasquez Mansilla, R. Zysler, D. Fiorani and L. Suber, Annealing effects on magnetic properties of acicular hematite nanoparticles, *Phys. B Condens. Matter*, 2002, **320**, 206–209.
60 C. Liu, H. Gao, L. Wang, T. Wang, X. Yang, P. Sun, Y. Gao, X. Liang, F. Liu, H. Song and G. Lu, Facile synthesis and the enhanced sensing properties of Pt-loaded α-Fe_2O_3 porous nanospheres, *Sens. Actuators, B Chem.*, 2017, **252**, 1153–1162.
61 N. Goel, K. Kunal, A. Kushwaha and M. Kumar, Metal oxide semiconductors for gas sensing, *Eng. Rep.*, 2023, **5**, e12604.
62 Y. Wang, S. Wang, Y. Zhao, B. Zhu, F. Kong, D. Wang, S. Wu, W. Huang and S. Zhang, H_2S sensing characteristics of Pt-doped α-Fe_2O_3 thick film sensors, *Sens. Actuators B Chem.*, 2007, **125**, 79–84.
63 F. Wang, K. Hu, H. Liu, Q. Zhao, K. Wang and Y. Zhang, Low temperature and fast response hydrogen gas sensor with Pd coated SnO_2 nanofiber rods, *Int. J. Hydrogen Energy*, 2020, **45**, 7234–7242.
64 S. M. Merah, Y. Bakha and A. Djelloul, N-type and P-type SnO_x thin films based MOX gas sensor testing, *J. Mater. Sci.: Mater. Electron.*, 2024, **35**, 250.
65 M. Zhu, H. Zhang, S. Zhang, H. Yao, X. Shi and S. Xu, Chemoresistive gas sensors based on noble-metal-decorated metal oxide semiconductors for H_2 detection, *Materials*, 2025, **18**, 451.
66 V. Shah, J. Bhaliya, G. M. Patel and P. Joshi, *Top. Catal.*, 2025, **68**, 1297–1337.
67 L. Liu and S. Liu, Oxygen Vacancies as an Efficient Strategy for Promotion of Low Concentration SO_2 Gas Sensing: The Case of Au-Modified SnO_2,, *ACS Sustain. Chem. Eng.*, 2018, **6**, 13427–13434.
68 Y. Wu, M. Yan, C. Tian, Y. Liu and Z. Hua, NO_2 Sensing Properties of Cr_2WO_6 Gas Sensor in Air and N_2 Atmospheres, *Front. Chem.*, 2020, **7**, 907.
69 R. Vyas, S. Sharma, P. Gupta, A. K. Prasad, S. K. Dhara, A. K. Tyagi, K. Sachdev and S. K. Sharma, Nitrogen dioxide induced conductivity switching in ZnO thin film, *J. Alloys Compd.*, 2013, **571**, 6–11.